Smart Structures and Systems, *Vol. 26, No. 6 (2020) 703-720*
DOI: https://doi.org/10.12989/sss.2020.26.6.703

An efficient vibration control strategy for reliability enhancement of HAWT blade

M. Mohamed Sajeer[1a], Arunasis Chakraborty[*1] and Sourav Das[2]

[1]Department of Civil Engineering, Indian Institute of Technology Guwahati, Assam, India
[2]School of Engineering, The University of British Columbia, Okanagan, Canada

(*Received October 27, 2019, Revised June 30, 2020, Accepted October 21, 2020*)

Abstract. This paper investigates the safety of the wind turbine blade against excessive deformation. For this purpose, the performance of the blade in the along-wind direction is improved by longitudinal stiffener made of shape memory alloy. The rationale behind the selection of this smart material is due to its ability to offer excellent thermo-mechanical behaviour at low strain. Here, Liang-Roger model is adopted for vibration control, and the super-elastic effects are utilised for blade stiffening. Turbulent wind fields are generated at the hub height using TurbSim and the corresponding loads are evaluated using blade element momentum theory. An efficient switching algorithm is developed along with performance curves that enable the designer to select an optimal mode of heating depending upon the operational scenario. Numerical results presented in this paper clearly demonstrate the performance envelope of the proposed stiffener and its influence on the reliability of the blade.

Keywords: wind turbine; shape memory alloy; BEM theory; cyclostationary analysis; crossing rate; semi-active control; reliability analysis

1. Introduction

The worldwide climate change in the recent past has forced mankind to opt for the alternate sources of renewable energy, e.g., wind energy, solar energy, wave energy. Among them, wind energy has witnessed popularity due to its commercial viability. The power produced by a wind turbine is proportional to its rotor area. Due to this reason, the rotor diameter of the modern megawatt turbines has grown larger, with flexible blades that undergo large amplitude vibration when exposed to aerodynamic loads. Besides fatigue and other associated issues, excessive deformation of the blade in the along-wind direction can lead to collision with the tower. To address this issue, rotors are often tilted with pre-cone angle, as shown in Fig. 1(a). IEC 61400-1 (2005) and DNVGL-ST-0376 (2015) outline the design guidelines for this purpose to avoid impact with the tower due to excessive deformation. However, tilting the rotor and slow-moving shaft in the drivetrain develops additional stress on the gear tooth and bedplate that ultimately induces damage and downtime for maintenance. It also generates additional stress at the root of the blades which need to be addressed in the analysis and design. The problem is more complex as the aerodynamic loads acting on the blades are cyclostationary in nature. So, its design must focus on two major issues - developing smart rotors that offer less deformation and analyse its performance due to cyclostationary aerodynamic loads. With this in view, the following sections review the literature on the vibration control and stochastic modelling/analysis of HAWT blades.

Vibration control of wind turbine blade has drawn researchers' attention in the recent past and the literature available on this topic outlines different options available for this purpose. Selection of an explicit vibration control device relies upon its performance, safety, compactness, capital expense, operational expense and maintenance requirements. Due to these reasons, most of the control devices used in mechanical and civil structures are not suitable for wind turbines. Among various techniques, load control is a popular method in the wind turbine industry to reduce fatigue load and increase the life span of a blade. There are several approaches proposed in the literature that includes both passive (viz. free yaw movement) and active (viz. blade pitch control) load control strategies (Van Dam *et al.* 2008). In this context, few advanced load control techniques are also proposed in the recent past, e.g., advanced pitch control, twist control, variable diameter rotor and active flow control (Rehman *et al.* 2018). Anderson and Bose (1983) have proposed pitch control to avoid damage of generator and gears during extreme wind and have incorporated a mode switching algorithm above the cut-off speed. Lackner (2013) have investigated the load control mechanism using variable power collective pitch controller for a floating offshore wind turbine. They have observed a 20% reduction of pitching motion of the platform, thereby similar increase of maximum power generation. Bossanyi (2003a) has studied individual pitch control using Linear Quadratic Gaussian (LQG) and Proportional Integral (PI) scheme to achieve a significant reduction of aerodynamic loads. In another paper, Bossanyi

---

[*] Corresponding author, Ph.D., Professor, E-mail: arunasis@iitg.ac.in

[a] Ph.D. Student, E-mail: sajeer.modavan@gmail.com

http://www.techno-press.org/?journal=sss&subpage=7

ISSN: 1738-1584 (Print), 1738-1991 (Online)

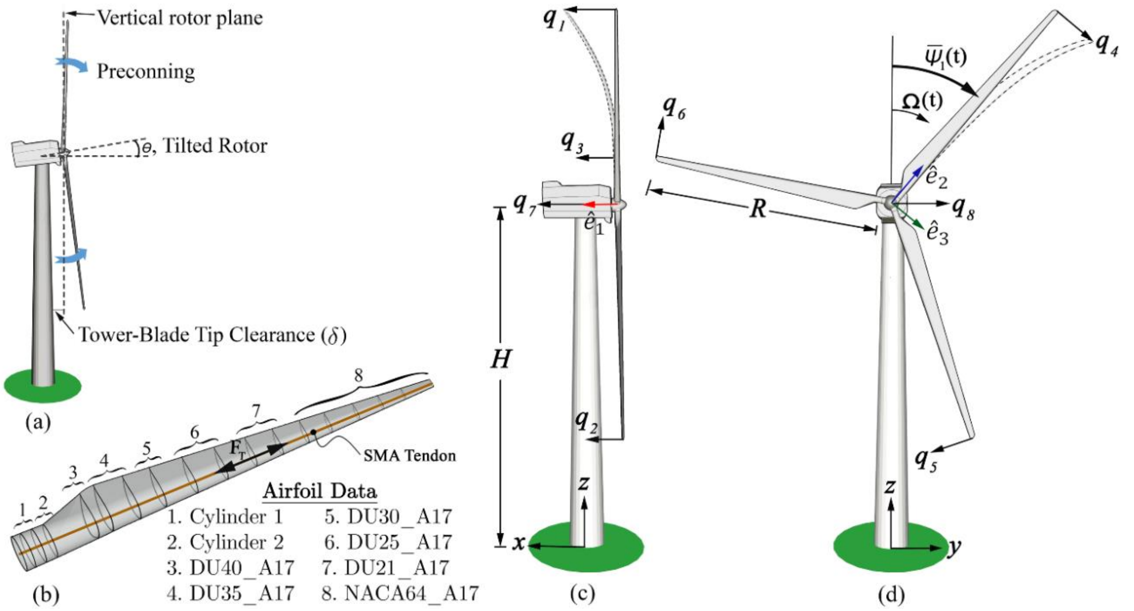

Fig. 1 Wind turbine model (a) tilting and pre-conning of blade; (b) airfoil distribution and centrifugal stiffener; (c) out-of-plane degrees of freedom and (d) in-plane degrees of freedom

(2003b) has presented a comprehensive review of different control strategies, including collective and individual pitch control. Agarwala and Ro (2015) have developed separate pitch control at the tip (SePCaT) of the blade to increase the power generation. They have compared the performance of their method using six different types of blades with SePCaT length varying from 5% to 30% of the blade length.

Besides pitch control, active flow control (Van Dam *et al*. 2008) also improves power generation of a wind turbine by reducing the extreme loads (e.g., trailing edge, synthetic jets, micro tabs, morphing and plasma actuators). Bottasso *et al*. (2016) have proposed passive flaps, which moves opposite to the blade vibration and works over a wider frequency range without affecting the power production. The advantage of this strategy is that it can be integrated with any other controllers and does not require sensors and actuators. Wilson *et al*. (2008) have proposed microtabs along with collective and individual pitch control to alleviate extreme loads, thereby, preventing damage and producing more energy. Their proposal has shown a 70% reduction of the root bending moment, which is also verified experimentally. The flow can also be controlled by ionising the surrounding air using Dielectric Barrier Discharge (DBD) plasma devices with the help of high electric potential. Nelson *et al*. (2008) have proposed a distributed DBD-plasma flow controller for wind turbine blades to increase the power output while reducing its vibration. It produces an ionic wind as soon as the electric field is applied that drives the nearby fluid. It also allows the designers to change the pitch distribution along the length of the blade as required for the optimal control. Thomas *et al*. (2009) have experimentally investigated the performance of DBD-plasma to improve the aerodynamic flow at a higher Reynolds number.

Above mentioned controllers do not change the shape of the airfoil and hence, the aerodynamic properties of the airfoil. In this context, blade morphing is an advanced technique often used to improve power production with an optimal profile to reduce extreme loads on the blade. It is mainly classified into in-plane morphing and out-of-plane morphing depending upon the direction of the shape modification. Lachenal *et al*. (2013) have demonstrated this concept with the details of shape adapting materials. They have discussed the possibilities of adapting different morphing concepts used in helicopter blades and aircraft wings. Berg *et al*. (2009) have investigated the effect of active aerodynamic load control using Grow-The-Rotor (GTR) and Trailing-Edge-Flap (TEF). GTR can retract the blade tip to reduce aerodynamic loads during extreme wind and can extend it to increase the power generation during normal condition. Their study has shown a 10-15% increase of power production with 10% increase of blade length. Wang *et al*. (2014) have proposed to apply a controllable linear blade twist along the length and have compared its performance with morphing and pitch control. Their study concludes that blade morphing performs better than pitch control in terms of power production. Cheng *et al*. (2015) have studied vibration control of blade using fibre-reinforced composite with visco-elastic damping layer, which significantly reduces vibration. Haghdoust *et al*. (2018) have investigated the passive damping of large wind turbine blades using thin SMA layer over the spar. They have modelled 89 m long DTU 10-MW wind turbine blade in ABAQUS and applied a thin CuZnAl SMA layer over the spar in three different configurations, which have offered significant improvement of blade damping. Küçük *et al*. (2012) have studied the stress development when different SMA (viz. Ni-Ti, Cu-Zn-Al and Cu-Al-Ni) materials are used in turbine root connection. Their study shows that nitinol gives better performance than other SMA materials in terms of von-Mises and yield stress. Das *et al*. (2019) have proposed longitudinal blade stiffening using SMA tendon to control the vibrations of large wind turbine blades. Thermodynamic properties of SMA are used to tune the control force, which shows a single stiffener can reduce blade vibration in both in-plane and out-of-plane directions.

Rotating mechanical systems often experience periodically varying non-stationary excitation. Although these systems can be studied using a general mathematical framework of non-stationary random vibration, their modelling comes under the special category of cyclostationary process. Gardner (1994) have studied the cyclostationarity of signals with major emphasis on its advantage and possible applications. Holm *et al.* (1995) have investigated the level crossing rate of a breathing crack under cyclostationary load on a fillet welded steel plate to study its effect on fatigue life. McCormick and Nandi (1998) have demonstrated the cyclostationary analysis of rotating machines to compare with stationary spectral analysis and first-order cyclic analysis (i.e., synchronous averaging). Antoni *et al.* (2004) have proposed a general guideline for modelling and analysis of rotating machines. They have shown that time-cyclostationarity of machine vibration exists when the velocity fluctuation is periodic as well as stationary. A comprehensive review of this topic is presented by Gardner *et al.* (2006). Chaari and Haddar (2014) have investigated the spectral analysis of wind turbine gear operating in a non-stationary environment. They have concluded that frequency-based analysis leads to erroneous results when the speed is non-uniform. Therefore, they have recommended a time-frequency analysis to model the variation in the frequency content of the response. Maheswari and Umamaheswari (2017) have reviewed the trends in the condition assessment of wind turbine drivetrain using cyclostationary analysis. In this context, bearing fault diagnosis of the drivetrain is a major issue in wind turbine industry (Ma *et al.* 2017). In this study, acceleration responses of the drivetrain bearings are used for fault detection in the inner and outer race, where the power spectrum and Cyclic Coherence Function (CCF) based signal processing is adopted. Teng *et al.* (2017) have applied CCF for fault analysis of wind turbine generator subjected to electro-magnetic vibration and compared with the demodulation ability of spectral kurtosis and complex wavelet transform. They have observed that CCF performs better than other methods available in the literature.

Structural reliability of the wind turbine blade is also investigated by several researchers in the recent past. Dimitrov *et al.* (2013) have estimated the reliability of composite wind turbine blade against blade-tower collision and fatigue failure. They have evaluated the safety factors using ultimate strength and fatigue limit state against the target reliability level. Jiang *et al.* (2017) have presented a comprehensive review of the structural reliability of a wind turbine blade. They have discussed the details of reliability analysis of mechanical and electrical components present in the nacelle. Liu *et al.* (2019) have studied the reliability of offshore floating wind turbine against excessive blade tip deformation and fatigue. They have investigated the effects of floating foundation on the failure probability of blade in comparison with the fixed foundation and observed that the probability of failure is significantly higher for a floating foundation.

1.1 Problem formulation

The literature review presented above highlights the recent trends in vibration control and cyclostationary analysis for the design of smart rotor. In this context, the performance of a controller under cyclostationary loading has remained an open problem, where excessive deformation is a major concern for fatigue life and impact with tower that can lead to catastrophic failure of the complete system (Ma *et al.* 2019). Thus, both IEC 61400-1 (2005) and DNVGL-ST-0376 (2015) have specific guidelines for sufficient clearance between blade and tower. In general, this is achieved by angular adjustment (i.e., tilt and precone) of the blades with little reduction in power production (Burton *et al.* 2011). But it imposes additional stress on the gear tooth and blade/shaft connections. In the recent past, many blades have failed due to this fastening problems. Branner and Ghadirian (2014) have summarised different wind turbine failure and identified the blade-tower collision under severe damage category. Hence, level crossing analysis is an integral part for the safe design and operation of these rotors. With this in view, the present study aims to address the following issues:

- Develop an efficient semi-active algorithm for vibration control of large wind turbine blade using SMA based longitudinal stiffening. The temperature of the material is proposed to be adjusted to generate the maximum allowable control force.
- Investigate the cyclostationary characteristics of blade response with and without the proposed longitudinal stiffener. Wavelet-based time-frequency analysis is proposed for quantifying the instantaneous frequency content and second-order moment statistics of the blade response.
- Inspect the reliability of the proposed blade stiffening against excessive deformation. This requires the formulation of the level crossing problem in the light of the cyclostationary nature of blade vibration.

2. Dynamics of onshore wind turbine

This work is primarily focused on the time-dependent reliability analysis of a wind turbine against bending deformation. For this purpose, a discrete model of the tower-blade assembly stiffened by SMA tendon is used here. It is discussed in this section, with only relevant equations presented for completeness. The reader may refer to Das *et al.* (2019) for the details of this model, which is also briefly mentioned in the Appendix.

The degrees of freedom of this model is shown in the schematic diagram of Fig. 1. Let $u(t)$ be the displacement of the system, which is defined as $u(t) = [u_i(t)] = \Phi_i q_i(t)$, $i = 1, 2, \dots, 8$ where Φ_i is the mode shape of the respective element (i.e., tower or blade) and q_i represent the degrees of freedom used in this analysis. It may be noted that the tower-nacelle assembly is modelled by two translational degrees of freedom, i.e., q_7 and q_8. The mass of each blade at a section r from the root is given by $m_b(r)$, which varies over its length R. In this analysis, only one mode of both tower and blade in two orthogonal directions are considered for modelling. However, the formulation is general and higher modes can be easily incorporated if it is necessary. The mass of the tower is expressed by $m_t(h)$ that varies over its height H and the nacelle-hub mass M_n is placed at the top of the tower. Therefore, the kinetic energy of the whole system is given by

$$\begin{aligned} T = & \underbrace{\frac{1}{2}\sum_{i=1}^{3}\int_0^R m_b(r) v_{b_i}^2(r,t)\,dr}_{\text{Blade}} \\ & \underbrace{+\frac{1}{2}M_n v_n^2(H,t) + \frac{1}{2}\int_0^H m_t(h) v_n^2(h,t)\,dh}_{\text{Tower}} \end{aligned} \tag{1}$$

In the above equation, v_n and v_b represent the velocities, where subscripts n and b correspond to the nacelle and blade, respectively. These velocities can be obtained from the displacement field u. Fig. 1(b) shows the SMA tendon that runs along the longitudinal axis of the blade to strengthen it. The tendon force F_T is developed to opposes the deformation of the blade. So, the potential energy of the combined blade-tower system is given by

$$\begin{aligned} V = & \underbrace{\frac{1}{2}\sum_{i=1}^{3}\int_0^R \left\{EI_f(r)\left(\frac{\partial^2 u_i}{\partial r^2}\right)^2 + EI_e(r)\left(\frac{\partial^2 u_{i+3}}{\partial r^2}\right)^2 + 2EI_{fe}(r)\frac{\partial^2 u_i}{\partial r^2}\frac{\partial^2 u_{i+3}}{\partial r^2}\right\}dr}_{\text{Blade (Elastic)}} + \underbrace{\frac{1}{2}\sum_{i=1}^{3}\int_0^R F_c(r)\left\{\left(\frac{\partial u_i}{\partial r}\right)^2 + \left(\frac{\partial u_{i+3}}{\partial r}\right)^2\right\}dr}_{\text{Blade (Centrifugal)}} \\ & + \underbrace{\frac{1}{2}\sum_{i=1}^{3}\int_0^R F_g(r)\left\{\left(\frac{\partial u_i}{\partial r}\right)^2 + \left(\frac{\partial u_{i+3}}{\partial r}\right)^2\right\}dr}_{\text{Blade (Gravitational)}} + \underbrace{\frac{1}{2}\left(k_{t_x}u_7^2 + k_{t_y}u_8^2\right)}_{\text{Tower}} + \underbrace{\frac{1}{2}\sum_{i=1}^{3}\int_0^R F_T(r)\left\{\left(\frac{\partial u_i}{\partial r}\right)^2 + \left(\frac{\partial u_{i+3}}{\partial r}\right)^2\right\}dr}_{\text{SMA Tendon}} \end{aligned} \tag{2}$$

where $F_c(r)$ and $F_g(r)$ are the forces due to the centrifugal acceleration and gravitation field. Parameters k_{tx} and k_{ty} are the out-of-plane and in-plane stiffnesses of the tower, respectively. The flexural rigidity of these two directions are expressed by EI_f and EI_e, respectively, while EI_{fe} is the interaction between them. The details of these sectional properties are omitted here to avoid repetition. The reader may refer to Sarkar and Chakraborty (2017) or Fitzgerald *et al.* (2018) for further information on this issue. Using Eqs. (1) and (2), the governing equation of motion can be derived using Lagrange's equation in the following compact form

$$M(t)\ddot{q}(t) + C(t)\dot{q}(t) + K(t)q(t) = F(t) \tag{3}$$

where $M(t)$, $C(t)$ and $K(t)$ are the time-dependent mass, damping and stiffness matrices, respectively. The components of these matrices are provided in the Appendix. $F(t)$ is the force vector acting on the turbine.

The damping force acting in this case consists of structural and aerodynamic components, where constant values of modal damping of tower and blade are assumed to act on the system. Although real-time aeroelastic simulation provides actual aerodynamic damping acting on the blades, equivalent modal damping is assumed in this study as recommended by Burton *et al.* (2011). Using this approximate formulation, the aerodynamic damping of the tower is obtained from the blades. Therefore, the total damping ratio of the blade and tower are evaluated as

$$\xi_i^b = \xi_i^{bs} + \xi_i^{ba} \qquad i = 1, 2, \ldots, 6 \tag{4a}$$

$$\xi_i^t = \xi_i^{ts} + \xi_i^{ta} \qquad i = 7\ \&\ 8 \tag{4b}$$

The first superscript b and t in Eq. (4) represent blade and tower, respectively while the second superscript s and a correspond to the structural and aerodynamic components. The subscript i in Eq. (4) denotes the mode of vibration.

2.1 Material model of SMA for centrifugal stiffening

In this study, shape memory alloy is used for the centrifugal stiffening of the blade, where the control strategy developed earlier by the authors (Das *et al.* 2019) is extended for efficient switching and reliability enhancement of blade. Therefore, only relevant equations necessary to describe the semi-active switching is presented here for completeness and continuity.

SMA changes its underlying microstructural orientation when exposed to temperature or electro-magnetic field. The ability to regain its predefined shape upon the application of heat is known as Shape Memory Effect (SME) while the ability to recover from large strain is known as the Super-elastic Effect (SE). Fig. 2(a) shows both SME (A-C-F-A) and SE (G-I-KG) in 3D stress-strain-temperature field, where A-B shows classical elastic deformation of this alloy. As the strain increases, twined martensite starts changing into detwined martensite, beyond this point (i.e., C) permanent plastic deformation can set in. Path C-D shows the elastic unloading in detwinned martensite phase with some residual strain depending on the level of loading, which can be removed by Joule heating, i.e., path D-E-F. The material regains its undeformed shape with zero martensite volume fraction (i.e., SME) above the austenite finish, i.e., A_f. Path F-A shows the cooling of SMA upon free stress condition, which brings the material back to its twinned martensite state again.

Once the temperature of the material reaches above A_f, stress-strain relation follows hysteresis in isothermal condition (i.e., SE) where path G-H shows classical elastic deformation in the austenite phase under moderate loading. Further increase of loading above the critical stress introduces stress-induced martensite (i.e., SIM) phase in the path H-I, followed by inelastic deformation along the path I-J. However, loading above this point leads to unrecoverable plastic deformation of the material. Path J-K

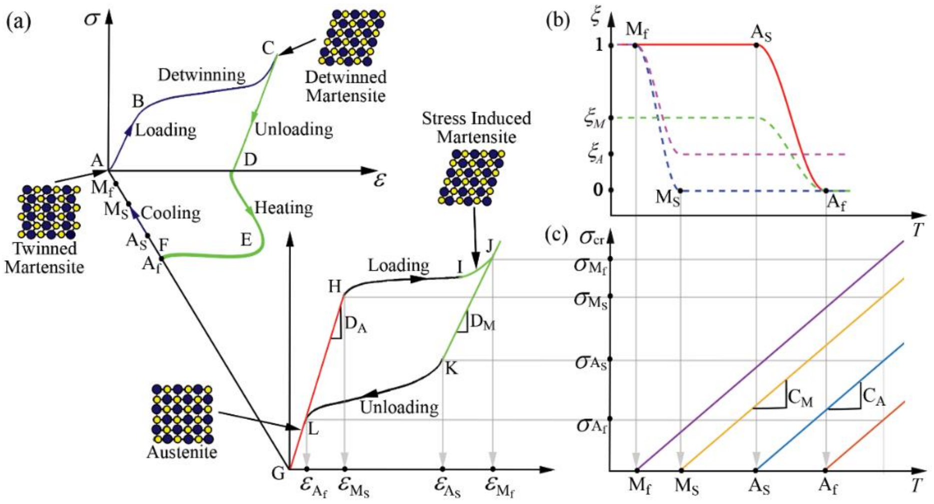

Fig. 2 Schematic representation of (a) stress-strain-temperature behaviour of SMA; (b) variation of martensite volume fraction and (c) variation of critical stress with respect to temperature

shows unloading of the stress so that thermo-dynamically stable austenite phase can start. Further unloading brings the material to austenite phase with the large recovery of strain (i.e., path K-L). Path L-M shows an ideal case of the strain recovery upon unloading. The reader may refer to Rao *et al*. (2015) for further details of this microstructural behaviour of SMA.

The super-elastic behaviour of SMA is exploited here to get the maximum possible control force. Among different models of stress-strain-temperature available in the literature, Liang and Rogers (1997) model is used, where, the behaviour of SMA is described as follows

$$\dot{\sigma} = D(\xi)\dot{\epsilon} + \alpha\dot{\xi} + \Theta\dot{T} \tag{5}$$

In the above equation, σ, ϵ, ξ and T are stress, strain, martensite volume fraction and temperature, respectively. Over dot in this expression represents derivative with respect to time, where D is Young's modulus of SMA, α is the phase transformation tensor and Θ is the thermoelastic tensor. Young's modulus of this material is a linear function of the martensite volume fraction. In this context, Fig. 2(b) shows a typical variation of martensite volume fraction with respect to temperature under free stress condition. Liang and Rogers (1997) have proposed cosine formula to describe this change in volume fraction during the phase transformation under free stress condition and suggests linear stress-temperature relation, as shown in Fig. 2(c). Here, it may be noted that the transformation temperatures (i.e., M_f, M_s, A_s and A_f) also vary linearly with stress and forms new boundaries (i.e., M_f^{σ}, M_s^{σ}, A^{σ}_s and A^{σ}_f), which may be obtained from the slope C_M and C_A. Using this model, the variation of martensite volume fraction can be expressed as a function of stress and temperature, i.e., $\dot{\xi} = \xi(\sigma, T)$. The volume fraction for the phase transformation from martensite to austenite is defined as follows

$$\xi = 0.5\xi_M\{\cos[A_A(T - A_s) + B_A\sigma] + 1\} \tag{6}$$

where T is the temperature of the current state when the phase transformation takes place. As the temperature decreases from M_s to M_f, the volume fraction is expressed as

$$\xi = \frac{(1 - \xi_A)}{2}\cos\left[A_M\left(T - M_f\right) + B_M\sigma\right] + \frac{(1 + \xi_A)}{2} \tag{7}$$

Parameters A_A, B_A, A_M and B_M in Eq. (6) are the material constants, whose details may be obtained from Das *et al*. (2019).

Above model of SMA is used in this study for reliability enhancement of turbine blades. The force developed in the SMA tendon can be adjusted by the application of heat as required during its operation, which follows the law of thermodynamics. The temperature of the SMA tendon gradually increases with the application of current and the heat is exchanged with the surrounding to maintain the equilibrium. Thus, net heat transfer $Q = Q_{gen} - Q_{out}$ to the tendon is expressed using the first law of thermodynamics as follows

$$\dot{Q} + \dot{W} = \dot{H} + \dot{\Pi}_P + \dot{\Pi}_K \tag{8}$$

In the above equation, W is the work done, Π_P and Π_K represent the potential and kinetic energy while H is the enthalpy. The rate of change of heat flow with respect to time depends on the rate of change of heat emitted and produced in the tendon with respect to time i.e., $\dot{Q} = \dot{Q}_{gen} - \dot{Q}_{out}$. The rate of heat generated due to the flow of current depends on the applied voltage (V) and the resistivity (ρ) of the stiffener whose length is L [i.e., $\dot{Q}_{gen} = (\rho L)^{-1}V^2A_{cr}$]. In this process, the rate of heat loss due to convection is $\dot{Q}_{out} = h_cA_{sur}\Delta T$, where h_c is the convective heat transfer coefficient and ΔT is the temperature difference with the surrounding. The rate of enthalpy due to phase transformation is a function of martensite volume fraction (Shahin *et al*. 1997), i.e., $\dot{H} = m\left(c_p\dot{T} - \Delta h\dot{\xi}\right)$, where m is the mass of the tendon, c_p and Δh represent the specific heat of the tendon and the latent heat of transformation, respectively. The rate of change of

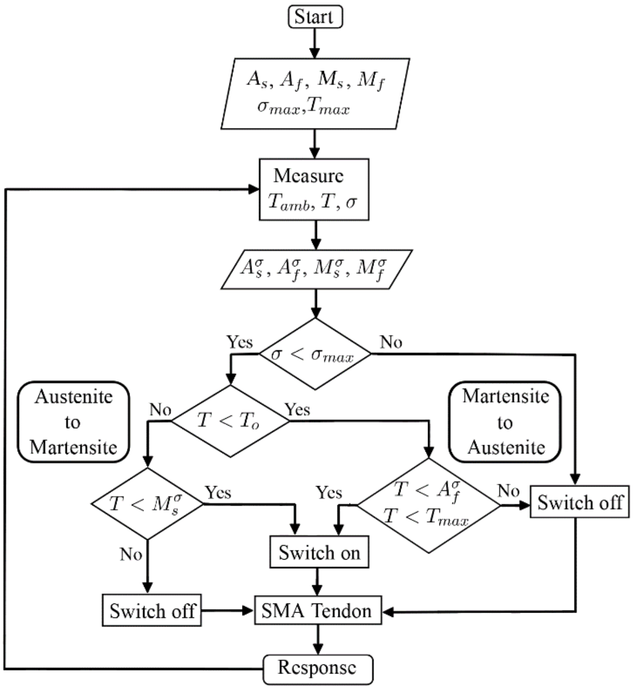

Fig. 3 Flow chart of the switching algorithm in semi-active case

potential energy is due to the amount of strain energy stored in the SMA tendon, i.e., $\dot{\Pi}_P = \sigma A_{cr}\dot{L}$ while the rate of change of kinetic energy is negligible and hence is considered zero, i.e., $\dot{\Pi}_K \approx 0$. Therefore, Eq. (8) can be modified into the following form

$$\frac{V^2 A_{cr}}{\rho L} - h_c A_{sur}\Delta T = m\left(c_p\dot{T} - \Delta h\dot{\xi}\right) + \sigma A_{cr}\dot{L} \tag{9}$$

The volume fraction in the above equation is a function of stress and temperature. Combining all these features, a generalised formula can be developed for the rate of change of stress and temperature with Joule heating as follows

$$\dot{\sigma} = \gamma_1\dot{\epsilon} + \gamma_2\dot{T} \tag{10}$$

$$\dot{T} = \frac{1}{\tau_2}\left[\frac{V^2 A_{cr}}{\rho L} - h_c A_{sur}(T - T_a) - \sigma A_{cr}\dot{L} - \tau_1\dot{\epsilon}\right] \tag{11}$$

In the above equation, $\gamma_1 = D(1 - \epsilon_L D E_2)^{-1}$ and $\gamma_2 = (\Theta + \epsilon_L D E_1)(1 - \epsilon_L D E_2)^{-1}$, where $\tau_1 = m\Delta h E_2\gamma_1$ and $\tau_2 = mc_p + m\Delta h(E_1 + E_2\gamma_2)$. As temperature increases, the material changes from martensite to austenite with $E_1 = A_A\chi$ and $E_2 = B_A\chi$, where χ varies with temperature and stress as follows

$$\chi = \begin{cases} \frac{\xi_M}{2}\sin[A_A(T - A_S) + B_A\sigma], & A_S + \frac{\sigma}{C_A} \le T \le A_f + \frac{\sigma}{C_A} \\ 0 & \text{Otherwise} \end{cases} \tag{12}$$

Similarly, the same parameters for decreasing temperature during austenite to martensite transform are $E_1 = A_M\chi$ and $E_2 = B_M\chi$, which is given by

$$\chi = \begin{cases} \frac{1-\xi_A}{2}\sin\left[A_M\left(T - M_f\right) + B_M\sigma\right], \\ \qquad M_f + \frac{\sigma}{C_M} \le T \le M_S + \frac{\sigma}{C_M} \\ 0 \qquad \text{Otherwise} \end{cases} \tag{13}$$

Using the above model of SMA, F_T in Eq. (2) is evaluated at every time instant, which acts against the longitudinal deformation of the blade.

2.2 Aerodynamic response of blade-tower assembly

The reduced degrees of freedom model of the combined system stiffened by the SMA tendon is used to study the reliability against bending deformation. The combined system is express in state-space using the state vector $Z = [q\ \dot{q}\ T\ \sigma]^T$ in the following form

$$\dot{Z} = A(t)Z(t) + B(t)W(t) \tag{14}$$

In Eq. (14), $W(t)$ is the combined aerodynamic and gravitational force vector, where the time-varying system matrix $A(t)$ and influence matrix $B(t)$ are as follows

$$A(t) = \begin{bmatrix} 0 & I \\ -M^{-1}(t)(K(t) + K_T(t)) & -M^{-1}(t)C(t) \end{bmatrix} \tag{15a}$$

$$B(t) = \begin{bmatrix} 0 \\ -M^{-1}(t)I \end{bmatrix} \tag{15b}$$

It may be noted here, $K_T(t)$ in Eq. (15a) represents the stiffness due to SMA tendon, which offers the control force $F_T(t) = \sigma(t)A_{cr}(t)$ to oppose the blade deformation.

Using the above mathematical model of the combined system, responses are evaluated, where thermo-mechanical properties of SMA are utilised to reduce the blade deformation. For this purpose, the feedback (i.e., T & σ) is utilised to evaluate the voltage to maintain the maximum possible control force. The flow chart of the proposed control algorithm is shown in Fig. 3. The phase transition temperature bounds of SMA and their design limits, which include maximum temperature and maximum stress, are defined as the initial input. The maximum design stress depends on the maximum recovery stress of the SMA tendon. A lesser value of stress than its allowable limit is selected as the maximum design stress to avoid any material damage. Similarly, the maximum design temperature is selected based on the allowable temperature of SMA and the surrounding materials to avoid any damage.

The time-dependent stress and temperature of SMA tendon are used and the revised (or stress-induced) thermal bounds of SMA ($M_f^\sigma, M_s^\sigma, A_s^\sigma, A_f^\sigma$) are evaluated using initial inputs and feedback. The current supply is switched on if the temperature is less than the bounds A_f^σ or $T_{\max}$. Here, it may be noted that the allowable stress limit of SMA increases in presence of electricity and thus the tendon offers more control force. The flow of current is continued until the temperature reaches its allowable limit (i.e., A_f^σ or $T_{\max}$) or the stress reaches its maximum design limits. Under this condition, current flow is discontinued, which initiates the fall of temperature and subsequently the stress offered by the tendon. So, the stress level reduces and as soon as the temperature goes below M_s^σ, the current supply is restored. Also, during switching, the martensite volume fraction is evaluated at every time instant based on the stress and temperature, as explained in section 2.1. Then the time derivative of stress and temperature are evaluated using Eqs. (10) and (11). Finally, the system responses, including stress and temperature of SMA tendon, are evaluated by solving Eq. (14).

2.3 Wavelet-based cyclostationary analysis and level crossing

In this section, cyclostationary analysis of the blade response is carried out to quantify its moment statistics. Turbine blades rotating at a constant speed in turbulent wind experience periodically varying aerodynamic loads, which lead to periodically varying non-stationary (i.e., cyclostationary) output. In this context, it may be noted that the cyclostationary process is a special case of a non-stationary process, which can be modelled and analysed in three different ways:

1. Close form solution (i.e., input-output relation) within the non-stationary framework.
2. Monte-Carlo or other advanced simulations to quantify the blade response statistics.
3. Time-frequency analysis or other signal-processing tools (e.g., time series), for statistical quantification.

The first option is not applicable in this case as the governing differential equation has time-dependent coefficients, which makes it difficult for a closed-form solution. As an alternative, large scale simulation is extremely time-consuming and is often impractical for field problems involving flow simulation. The last option has a trade-off between the other two, which also offer clear insight into the instantaneous frequency content of the signal. Hence, it is adopted in this study, where wavelet-based time-frequency analysis is used to characterise the response statistics. With this in view, a brief overview of the continuous wavelet transform and its use for cyclostationary response analysis of HAWT blade is presented below, which is followed by time-dependent reliability assessment.

Let, $f(t)$ be a continuous-time signal in $L^2\mathbb{R}$ whose amplitude and frequency content varies with time. The continuous wavelet transform of this signal is given by (Chan 1995).

$$W_\psi f(a,b) = \int_{-\infty}^{+\infty} f(t)\psi_{a,b}^*(t)dt \tag{16}$$

In the above equation, $*$ indicates complex conjugate while $\psi_{a,b}(t)$ represents the shifted and dilated versions of the mother wavelet $\psi(t)$ in the following form.

$$\psi_{a,b}(t) = \frac{1}{|a|}\psi\left(\frac{t-b}{a}\right) \qquad a,b \in \mathbb{R}^+ \tag{17}$$

It may be noted that parameter a controls the filter width by adjusting its frequency content while the other parameter b localises $\psi(t)$ to extract the instantaneous features of $f(t)$. Eq. (16) is digitally evaluated by discretising the scale and time parameters in the following way

$$\Delta a_j = \frac{1}{2}\left[\left(a_{j+1} - a_j\right) - \left(a_j - a_{j-1}\right)\right] = \frac{a_j}{2}\left(\sigma - \frac{1}{\sigma}\right) \tag{18a}$$

$$\Delta b_\kappa = \frac{1}{2}\left[(b_{\kappa+1} - b_\kappa) - (b_\kappa - b_{\kappa-1})\right] = \Delta b \tag{18b}$$

In the above equations, $a_j = \sigma^j$ and $b_\kappa = (\kappa - 1)\Delta b$. Thus, the time discretised version of the inverse wavelet transform for the point-wise reconstruction of the original signal is given by the following form.

$$\begin{aligned} f(t) &= \frac{1}{2\pi C_\psi}\int_{-\infty}^{+\infty}\int_{-\infty}^{+\infty} \frac{1}{a^2} W_\psi f(a,b)\psi_{a,b}(t)da db \\ &= \sum_j\sum_\kappa \frac{K\Delta b}{a_j} W_\psi f\left(a_j, b_\kappa\right)\psi\left(\frac{t-b_\kappa}{a_j}\right) \end{aligned} \tag{19}$$

In this study, complex Morlet wavelet is used, which is mathematically described by the following expression.

$$\psi(t) = \frac{1}{\sqrt{\pi f_b}}\exp(i2\pi f_c t)\exp(-t^2/f_b) \tag{20}$$

Parameters f_c and f_b represent the central frequency and frequency bandwidth of the mother wavelet.

Once the original signal is transformed into the time-frequency domain, instantaneous moment statistics can be obtained easily. Thus, applying expectation operator on both sides of Eq. (19), the time-dependent mean of $f(t)$ can be evaluated as follows.

$$\begin{aligned} \mu_{f(t)} &= E[f(t)] \\ &= \sum_j\sum_\kappa \frac{K\Delta b}{a_j} E\left[W_\psi f\left(a_j, b_\kappa\right)\right]\psi\left(\frac{t-b_\kappa}{a_j}\right) \end{aligned} \tag{21}$$

Similarly, the instantaneous second-order moment of the signal $f(t)$ can be obtained by taking the inner product of it, which can be expressed in the following form.

$$\begin{aligned} \langle f(t).f(t)\rangle &= \int_{-\infty}^{+\infty} f^2(t)dt \\ &= \frac{1}{2\pi C_\psi}\int_{-\infty}^{+\infty}\int_{-\infty}^{+\infty} \frac{W_\psi^2 f(a,b)}{a^2} da\, db \\ &= \sum_j\sum_\kappa \frac{K\Delta b}{a_j} W_\psi^2 f\left(a_j, b_\kappa\right) \end{aligned} \tag{22}$$

Here, it may be noted that the wavelet transform in Eq.

(16) localises the basis function at around $t = b_\kappa$ at a scale a_j, which has an effective bandwidth depending upon the type of the basis function used in this transformation. Therefore, the instantaneous value of the second moment of $f(t)$ can be quantified by the following expression.

$$E[f^2(t)]]|_{t=b_\kappa} = \sum_j \frac{K}{a_j} E\left[W_\psi^2 f\left(a_j, b_\kappa\right)\right] \tag{23}$$

Eqs. (21) and (23) are applicable for any non-stationary signal as encountered in this work. This is also applicable for cyclostationary process, where the frequency content of the signal varies with a dominant frequency as in case of a horizontal axis wind turbine. This wavelet-based time-frequency analysis has witnessed different applications in wind turbine design. For example, wavelet-based pitch controllers are used to enhance the performance of the wind turbine system, as reported by Fitzgerald *et al.* (2019) and Sarkar *et al.* (2020). However, in this study, it is used in stochastic sense to investigate the cyclostationarity of the blade vibrations.

Once the instantaneous first and second moments are evaluated, they can be used further for time-dependent reliability analysis. As stated in the objectives, the focus of this study is to improve blade deformation to avoid impact with the tower, which leads to catastrophic consequences. To avoid this issue, blades have pre-cone at the hub, as shown in Fig. 1(a), where clearance between the tower and blade (i.e., δ) should be sufficient to accommodate the tip deflection of the blade in the along-wind direction. This level crossing problem is addressed by the SMA stiffener that runs along the axis of the blade, which can avoid the precone angle. So, the non-stationary along-wind response X_i exhibits a positive up-crossing rate of $\nu_{X_i}^+(\delta, t)$ within the time interval $(0,t]$, which is given by the following expression (Lutes and Sarkani 2004).

$$\nu_{X_i}^+(\delta, t) = \int_0^\infty v_i(t) p_{X(t),\dot{X}_i(t)}(u_i, v_i) dv_i \quad i = 1, 2, 3 \tag{24}$$

Above formulation demands the parent process $X_i(t)$ be narrow banded to quantify the peak distribution. This is logical for a wind turbine considered in this study as the along-wind cyclostationary blade tip response is primarily narrow banded, where the rotational frequency of the turbine dominates the response. This will be further demonstrated in the numerical analysis. Now, Eq. (24) can be simplified in the following form if the parent process is Gaussian (Lutes and Sarkani 2004) with time-varying mean and standard deviation.

$$\nu_{X_i}^+(\delta, t) = \frac{1}{\sqrt{2\pi}\sigma_{X_i}(t)} \exp\left[-\frac{1}{2}\left\{\frac{X_i(t) - \mu_{X_i}(t)}{\sigma_{X_i}(t)}\right\}^2\right] \left[\mu_{X_i}(t)\Phi\left(\frac{\mu_{\dot{X}_i}(t)}{\sigma_{\dot{X}_i(t)}}\right) + \frac{\sigma_{\dot{X}_i(t)}}{\sqrt{2\pi}}\right] \tag{25}$$

Time-dependent mean and standard deviation in the above equation are represented by $\mu(t)$ and $\sigma(t)$ while the parent process and its derivative have the nomenclature X_i and $\dot{X}_i$, respectively, where $\Phi(.)$ represents the standard normal CDF. Since the time of occurrence of the extreme event is rare, it can be modelled as a Poisson process (Lutes and Sarkani 2004). Using this model of a discrete event within the time interval $(0,t]$, the probability of occurrence of n up-crossing can be expressed as

$$P(n, t) = \frac{\nu_{X_i}^+(\delta, t)t}{n!} \exp(-\nu t) \tag{26}$$

Hence, the probability of no crossing (i.e., reliability) in the given time interval can be estimated using the above expression for different models (i.e., blade without and with SMA stiffener). This will be evaluated in the following numerical analysis to demonstrate the performance of the proposed SMA stiffener.

3. Numerical results and discussion

In this section, the reliability analysis using the proposed blade stiffening strategy is presented. The reduced degrees of freedom model of the turbine is developed using benchmark 5-MW NREL data (Jonkman *et al.* 2009), which is shown in Table 1. It has three blades of length 61.5 m connected to the hub of diameter 3 m, thus, forming the total rotor diameter of 126 m located at the height of 90 m from the ground. It is designed for 3 m/s cut-in and 11.4 m/s rated wind speeds with the corresponding revolution per minutes are 6.9 rpm and 12.1 rpm, respectively. Above the rated wind speed, the pitch angle of the blade is adjusted to maintain the rpm. Finally, the breaks are applied at the cut-out speed of 25 m/s. The blade has eight different airfoils distributed from the root to the tip, as shown in Fig. 1(d). The details of distributed parameters like mass per unit length, bending stiffness and aero-twist used in this analysis can be obtained from Jonkman *et al.* (2009). The natural

Table 1 NREL 5-MW turbine data Jonkman *et al.* (2009)

Basic descriptions		Blade		Tower	
P_{Rated}	5 MW	R_b	61.5 m	H_t	87.6 m
H_h	90 m	f_{flap}^b	0.66 Hz	$f_{\text{fore-aft}}^b$	0.324 Hz
D_h	3 m	f_{edge}^b	1.08 Hz	$f_{side-to-side}^b$	0.312 Hz
v_{ci}, v_r, v_{co}	3 m/s, 11.4 m/s, 25 m/s	ξ_b	0.477%	ξ_t	1%
rpm_{ci}, rpm_r	6.9 rpm, 12.1 rpm	N_b	3	M_h, M_n	56780 kg, 240000 kg

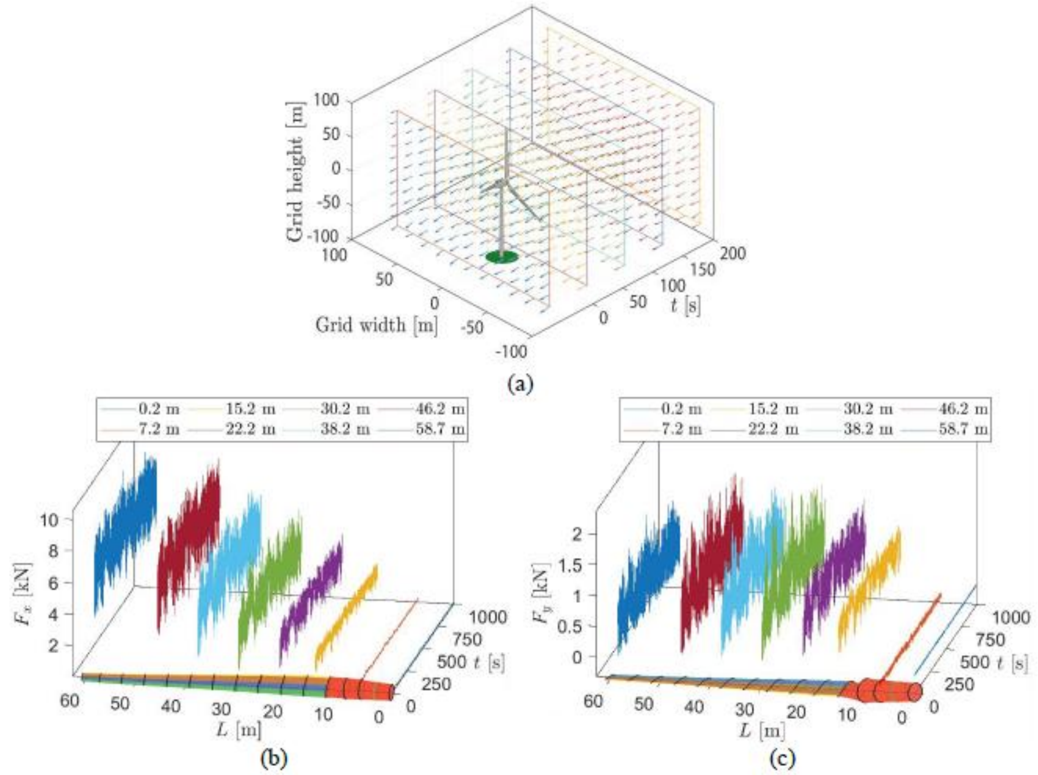

Fig. 4 Wind field and aerodynamic loads (a) wind flow at rated speed; (b) aerodynamic loads in out-of-plane and (c) aerodynamic loads in in-plane [NB: Blade orientation is schematic, not having exact pitch and aero-twist w.r.t load]

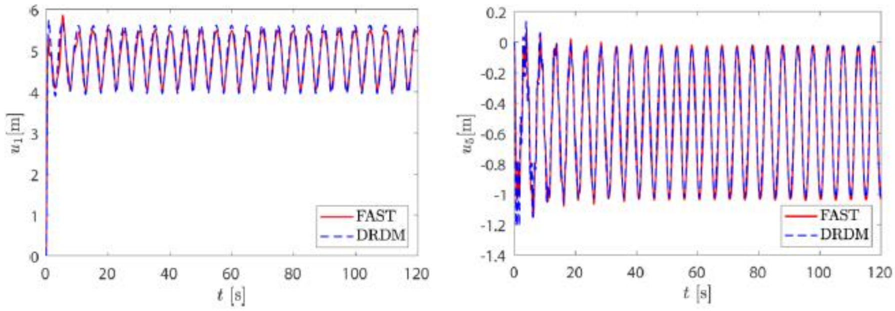

(a) (b)

Fig. 5 Displacement time history of the wind turbine blade at 11.4 m/s steady wind flow; (a) out-of-plane and (b) in-plane [DRDM → discrete reduced degrees of freedom model]

frequencies of the blade in the flapwise and edgewise directions are 0.667 Hz and 1.08 Hz, respectively, with 0.477% structural damping ratio in these modes. The frequency of the tower in the fore-aft and side-to-side directions are 0.312 Hz and 0.324 Hz, respectively, with 1% structural damping ratio in all the tower modes.

3.1 Wind load generation and response validation

The wind field is generated at the hub height using TurbSim (Jonkman 2009) for the rated speed of 11.4 m/s with 15% turbulence, as shown in Fig. 4(a). It is a full field turbulent wind simulation software developed by NREL that generates three components (Downwind, crosswind and vertical wind) at any point in a rectangular grid around the hub. In this study, Kaimal spectrum is used to generate the wind field. Aerodynamic loads at 48 points on the blade are evaluated from the wind field using Blade Element Momentum (BEM) theory. Figs. 4(b) and (c) show the loads acting on the blade at a few selected nodes in the out-of-plane and in-plane directions, respectively. The tower loads in these two directions are mainly contributed by the blades, i.e., net blade loads acting at the nacelle.

The time-varying mass, stiffness and damping matrices as described in section 2 are evaluated to find the response of the combined system. To validate the model, aeroelastic simulation software developed by NREL, i.e., FAST (Jonkman and Buhl 2005) is used here. A steady wind flow

Table 2 Properties of SMA

Mechanical properties		Physical properties		Thermodynamic properties	
ρ_d	6450 kg/m^3	A_s	34.5°C	c_p	450 J/kg-K
$D_A - D_M$	83-28 GPa	A_f	49.0°C	Δh	30000 J/kg
$C_A - C_M$	13.8-13.8 MPa/K	M_s	18.4°C	h_c	10 W/m^{2}K
$\sigma_{\max}$	900 MPa	M_f	9.0°C	T_a	25°C
ϵ_L	0.067	Θ	0.55 MPa/K	ρ_r	1 μΩm

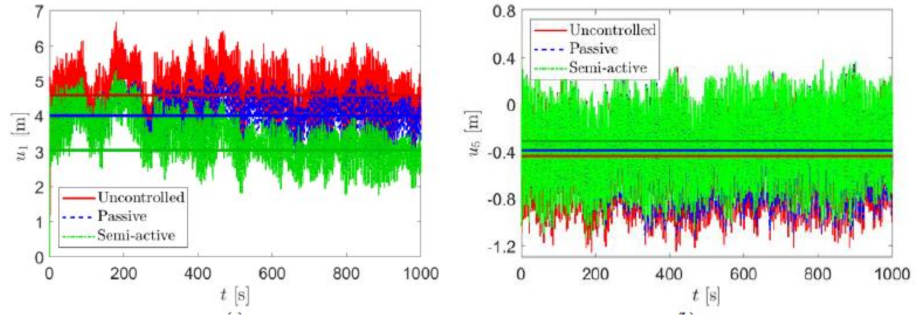

(a) (b)

Fig. 6 Blade response at 11.4 m/s wind speed with 25.4 mm diameter SMA tendon: (a) out-of-plane; (b) in-plane displacement time history [NB: Horizontal line shows the mean response]

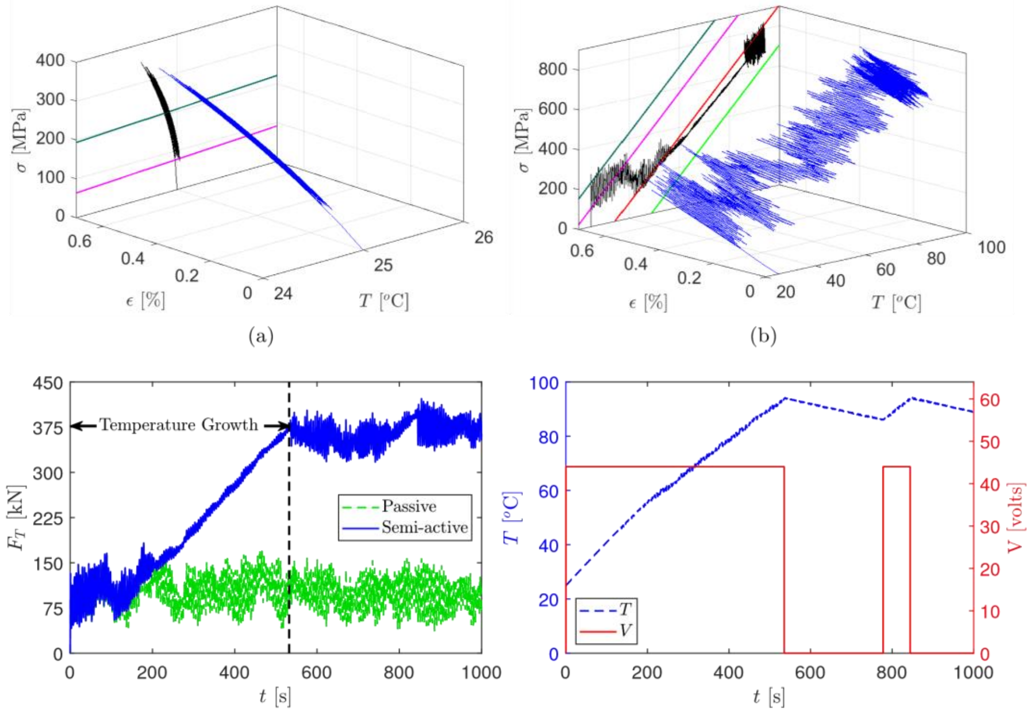

(a) (b) (c) (d)

Fig. 7 Stress and temperature variation of 25.4 mm diameter SMA tendon at 11.4 m/s average wind speed: (a) stress-strain-temperature in passive case; (b) stress-strain-temperature in semi-active case; (c) control force exerted by SMA tendon; and (d) temperature applied for semi-active control

at 11.4 m/s is generated using TurbSim and corresponding blade loads are estimated using BEM theory. The same wind field is also applied in FAST to generate the response of the wind turbine system. Fig. 5 shows the displacement at the blade tip in the out-of-plane and in-plane directions using the proposed discrete reduced degrees of freedom model (DRDM) and FAST. Here, it may be noted that the axial blade stiffening force is kept zeros for this validation

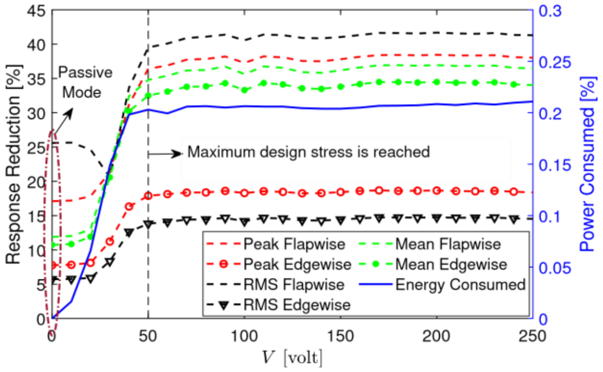

Fig. 8 Percentage reduction in blade response and energy consumption w.r.t. voltage at rated speed for 25.4 mm diameter tendon

exercise. It is observed that the reduced degrees of freedom model match closely with FAST and hence, can be used for further to study the SMA based vibration control and reliability analysis.

3.2 Semi-active switching for effective control

In this study, longitudinal stiffener (i.e., SMA tendon) is used to reduce the vibration of the blade, whose material modelling is discussed in section 2.1. Nitinol is used here for its excellent thermo-electro-mechanical properties, which are given in Table 2. The density of this material is 6450 kg/m^3 and Young's modulus in austenite and martensite phases are assumed to be 83 GPa and 28 GPa, respectively. The maximum recovery stress of nitinol is 900 MPa. The feedback stress is used after the application of voltage; hence maximum design stress needs to be defined to avoid crossing of the maximum recoverable stress. Here, 825 MPa is selected as the maximum design stress value. Crossing of this limit will switch off the current flow so that there is enough gap between this value and the maximum recovery stress. Also, the heating of the SMA tendon is limited up to 95°C in order to avoid damage to the surrounding materials. This value may change depending on the properties of the blade material and other design requirements, if any. The ambient temperature is assumed to be 25°C.

The response analysis of the wind turbine is carried out with and without stiffener (i.e., uncontrolled and passive or semi-active controlled) and the tip displacement of the blade is shown in Fig. 6 for comparison. In case of passive operation, zero voltage is applied to the SMA tendon while in the semi-active case, 44 V is applied with the option of switching. Figs. 6(a) and (b) show the displacement response in the two orthogonal directions. The tip displacement of the blade in the out-of-plane direction is very high compared to that in the in-plane direction. The maximum displacement in the along-wind direction is ~6 m while the same in the in-plane direction is ~1 m at the rated speed. Due to this reason, IEC 61400-1 (2005) and DNVGL-ST-0376 (2015) provide guidelines for tilt and pre-cone angle to the avoid impact with the tower. In this study, the blades are modelled with zero pre-cone, which indicates the blade-tower clearance is ~7.79 m. The tip displacement of the blade is reduced significantly due to the proposed longitudinal stiffener. The percentage of response reductions in this study are evaluated in different modes of operation over 1000 s in which the initial 450 s is used by the tendon to gain sufficient heating (~80°C) in semi-active mode. The figures show that peak displacement at the blade tip in the along-wind direction is reduced by 18.51% and 31.61% in passive and semi-active mode, respectively, while 5.69% and 12.75% peak displacement reduction are observed in the in-plane direction for the same mode of operations. Moreover, the mean components of the responses are also reduced significantly in both these directions when SMA stiffener is used. The mean reductions with SMA tendon in the out-of-plane blade tip responses are 12.59% and 33.50% in two different modes of operations, respectively, while the same stiffener offers 11.33% and 29.95% mean reduction in the in-plane direction. These are marked by the horizontal lines in Fig. 6. The RMS responses in the along-wind direction are reduced by 26.97% and 35.55% using passive and semi-active case, respectively, while the same in the in-plane direction are reduced by 6.00% and 12.45%, respectively.

The stress-strain-temperature behaviour of SMA tendon is shown in Figs. 7(a) and (b) for passive and semi-active case, respectively. In the passive case, the tendon temperature remains the same for all practical purpose compared to ambient temperature. Whereas, the temperature in the semi-active case increases with the application of current to achieve more control force, as shown in Fig. 7(c). The SMA material can undergo ~6-8% strain; however, the maximum strain observed in both these cases are close to 1%. This is due to the fact that the stiffener prevents blade deformation, which is reflected in the lower axial strain. This also justified the use of SMA, which can offer large allowable stress compared to other materials in that strain range. As the current flow is switched on, the temperature is permitted to increase up to the allowable limit at around 530 s. Then the current is switched off and the tendon temperature starts to decrease slowly depending on the surrounding condition as shown in Fig. 7(d). In this study, convective heat transfer coefficient is considered to be 10 W/m^{2}K for air-free convection and the thermal conductivity of the SMA tendon are 8.6 W/mK and 18 W/mK for martensite and austenite phase, respectively. The heating is switched on when the temperature drops by 10°C to maintain the required control force. This analysis is further continued to study the power failure during turbulent wind flow, which is a common critique for any semi-active or active control strategy. The advantage of the proposed algorithm lies in its ability to perform satisfactorily in the passive mode in case of a power failure, where it can still offer significant response reduction. This indicates that a minimum level of control is guaranteed by the proposed algorithm.

A sensitivity analysis is carried out to study the performance of the SMA stiffener under various applied voltages and the results are shown in Fig. 8, where the zero voltage (i.e., the initial case) represents the stiffener in passive mode. The percentage reduction of peak and mean

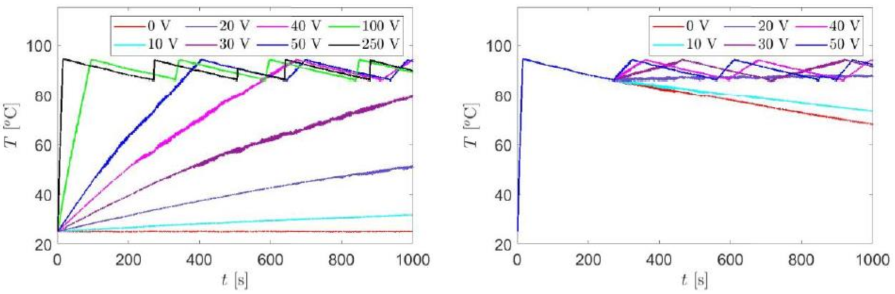

(a) (b)

Fig. 9 Temperature variation of 25.4 mm diameter tendon for different voltage; (a) initial temperature = 25°C and (b) initial temperature = 85°C

Table 3 Peak, mean and RMS response reduction in out-of-plane and in-plane directions

Type	d (mm)	Out-of-plane Peak (%)	Out-of-plane Mean (%)	Out-of-plane RMS (%)	In-plane Peak (%)	In-plane Mean (%)	In-plane RMS (%)
Passive	12.70	6.26	3.98	9.51	2.84	3.58	2.06
	25.40	17.10	11.90	25.59	7.77	10.74	5.73
	38.10	26.44	19.69	38.51	12.13	17.82	8.97
	50.80	33.76	26.34	47.82	15.44	23.93	11.58
Semi-active	12.70	11.86	10.99	13.59	5.88	10.22	4.22
	25.40	34.65	33.84	37.70	17.34	31.60	13.37
	38.10	53.52	53.68	55.73	28.68	50.48	23.73
	50.80	66.68	67.19	68.30	42.90	63.71	35.88

*N.B.: Above results are based on ensemble average

+displacement response in both these directions increase drastically with the increase of voltage from 25 V to 50 V and become stable (i.e., very little change in percentage reduction on further increase of voltage as it has already reached its maximum allowable temperature). The power consumed by the proposed controller as the percentage of the rated power of the turbine is also shown in Fig. 8. It can be observed that the net power consumed by the SMA tendon in semi-active mode is 0.21% of the rated power, which is minimal for all practical purpose.

Further, the heating of tendon with different voltages are analysed to find the most favourable range for effective control with an initial temperature of 25°C, as shown in Fig. 9(a). It is observed that starting with 40 V needs 670 s to attain the maximum allowable temperature while with 50 V reaches the same within 400 s. Similarly, 100 V and 250 V initial current reach the same temperature level in 95 s and 17 s, respectively. This indicates that a higher initial voltage offers quicker heating to achieve the maximum allowable temperature, which needs frequent switching to maintain the control force.

To examine it further, an initial voltage of 250 V is applied to reach 95°C followed by switching. The current flow is restored after a temperature drop of 10°C, as shown in Fig. 9(b). The voltage, which can maintain the temperature and subsequently the stress level close to its design value, is selected as the effective voltage during switching operation. In this case, 20 V current flow is able to maintain the temperature at the required level without frequent switching. Hence, it is considered as the effective voltage for the semi-active mode, where initial voltage is 250 V. Here, it may be noted that the designer has the option to select the mode of operation, i.e., passive or semi-active. As the performance in passive mode is significant, it can be selected for regular operation, leaving the semi-active mode for extreme wind flow only. This will not only help to mitigate the demand for the extreme wind flow, i.e., gust, it will also help to increase the operational lifespan of the controller. In this context, the recent development of wind measurements can detect the impending gust on the rotor plane, e.g., LIDAR (Harris *et al*. 2006). The proposed controller can be integrated with such devices to offer optimal performance whenever necessary.

3.3 Level crossing and reliability analysis

Once the optimal performance of the controller is established, its efficiency under uncertain wind flow is studied further. For this purpose, an ensemble of 25 wind flow field is simulated and the BEM theory is invoked in each case to simulate the corresponding aerodynamic load. Using these loads, uncontrolled and controlled responses are simulated, and the performance of the proposed control strategy for different tendon diameter are summarised in Table 3. From this table, it can be noted that the percentage reductions of the peak, mean and RMS displacements in the two orthogonal directions increase with the increase of tendon diameter. It is also observed that the controller performs better in the out-of-plane direction as compared to the in-plane direction. This is due to the fact that the deformation in the in-plane direction is less compared to the along-wind direction, which leads to lower axial strain. As obvious, the performance of the controller in the semi-active mode is significantly better than that in the passive mode.

To study the reliability of the system against excessive blade deformation, the level crossing problem is solved. For this purpose, wavelet-based time-frequency analysis, as described in section 2.3, is invoked. Complex Morlet wavelet is used here, whose central frequency is 5 Hz. Fig. 10 shows the ensemble average of the wavelet coefficients

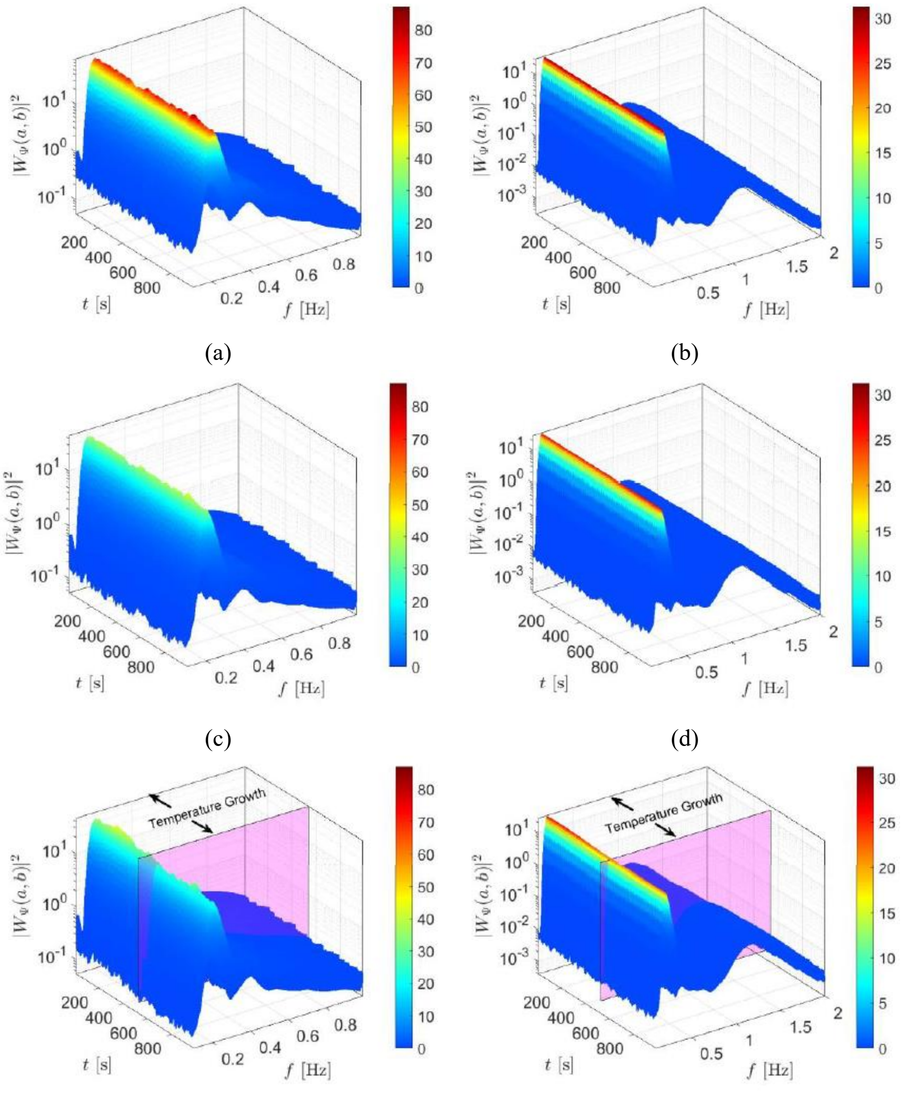

(a) (b)

(c) (d)

(e) (f)

Fig. 10 Wavelet coefficients of blade response at rated speed: (a) uncontrolled case in out-of-plane; (b) uncontrolled in in-plane; (c) passive case in out-of-plane; (d) passive case in in-plane; (e) semi-active case in out-of-plane; and (f) semi-active case in in-plane

of blade response in two orthogonal directions (i.e., out-of-plane and in-plane) under three different modes of operations (i.e., uncontrolled, passive and semi-active). This figure reveals that the response is cyclostationary, where the rotational frequency of the turbine dominates the response. Although the spectrograms show modal participation from flapwise and edgewise vibration, their contributions compared to the rotational frequency are significantly less. Furthermore, the amplitude of the expected value of the wavelet coefficients reduces in the passive mode as compared to the uncontrolled case. This reduction is more in the semi-active case, where the initial temperature growth is needed to reach the maximum allowable stress level.

Using these average wavelet coefficients, statistical moments of the blade tip response in the out-of-plane and in-plane directions are evaluated, which are shown in Fig. 11. From this figure, it can be concluded that the proposed control strategy offers considerable response reduction in terms of time-varying mean and standard deviation of the blade vibration. The level crossing problem is then solved, where the positive up crossing of the threshold (i.e., 7.79 m clearance between blade and tower) is considered for the different mode of operations. Eq. (25) shows the time dependence of the crossing rate when the underlying stochastic process is Gaussian. Thus, the nature of the response is studied before solving the crossing rate. For this reason, four different time points are selected arbitrarily and the ensemble response at these time instants are plotted in probability paper. These are shown in Fig. 12(a), which justify the assumption (i.e., Gaussianity) of the underlying stochastic process. Finally, the time-dependent crossing rate $\lambda^+(u, t)$ is evaluated, as shown in Fig. 12(b) for 25.4 mm diameter of the tendon. It clearly shows the improvement of the crossing rate from the uncontrolled to passive and semi-active mode. Using the maximum value of the crossing rate,

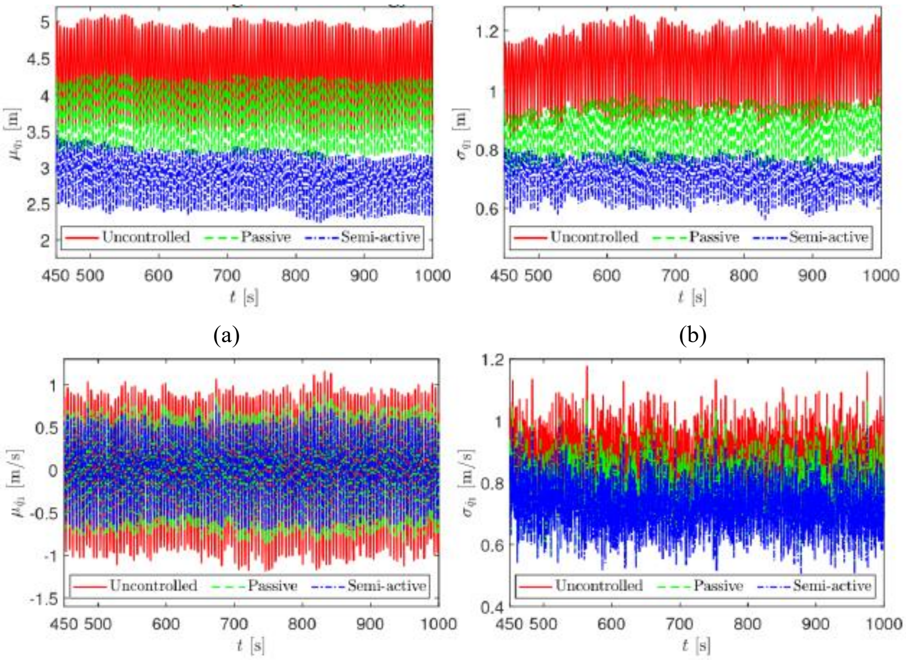

(a) (b)

(c) (d)

Fig. 11 Out-of-plane blade response at rated speed for 25.4 mm diameter SMA tendon: (a) mean of displacement time history; (b) standard deviation of displacement time history; (c) mean of velocity time history and (d) standard deviation of velocity time history

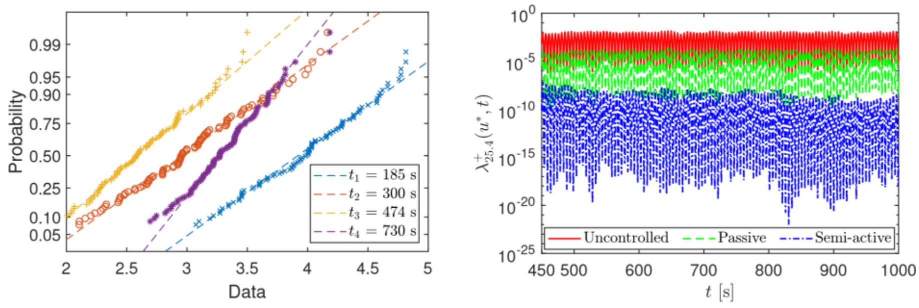

(a) (b)

Fig. 12 (a) Ensemble blade response in probability paper and (b) Crossing rate at rated speed for 25.4 mm diameter SMA tendon

the probability of occurrence within the given time interval is evaluated as described in Eq. (26). Table 4 shows the probability of zero-crossing (i.e., reliability) of the controller against allowable deformation limit. The numerical figure reported in this table clearly shows significant improvement of the reliability. This table also shows that performance of the controller during power failure (i.e., passive mode) is also significant, which is an added advantage with this strategy.

4. Conclusions

The importance of blade vibration control is ever increasing, especially for large new generation rotors, as they experience considerable along-wind deformation. With this in view, a 5MW onshore wind turbine subjected to the 11.4 m/s rated wind speed and 15% turbulence at the hub height is investigated with and without the controller. The discrete reduced degrees of freedom model of the turbine is used to simulate the response where SMA based longitudinal stiffener is proposed to mitigate the blade vibration. The material property of the tendon is modelled by combining Liang and Rogers constitutive law with the principles of thermodynamics. A voltage-based switching algorithm is developed to model the semi-active mode of operation. It is observed that the proposed stiffener has significantly improved the performance of blade. The major contributions in this work and the advantages of the proposed control strategy are as follows:

- The proposed controller can operate in both passive and semi-active mode. In the semi-active mode, an efficient switching algorithm is developed, where the initial voltage and the voltage during switching can be adjusted depending upon the demand. The controller can be designed in passive mode to meet the regular serviceability requirements while the semi-active mode can be invoked during any emergency. This offers flexibility to the operator for mode switching, where the minimum level of performance is always guaranteed. In this context, the power requirement in the semi-active mode is extremely low, which also advocates for its efficiency in semi-active mode.

• The paper also offers the mathematical framework for cyclostationary analysis of blade response. The numerical study clearly shows the cyclostationary nature of the response, where rotational frequency predominates over other structural frequencies. The wavelet-based time-frequency analysis offers a perfect solution to model the instantaneous frequency content of the response. Using these wavelet coefficients, time-varying response statistics can be quantified, which is otherwise difficult for wind turbine system using conventional input-output relation in non-stationary random vibration framework as the system matrices are time-dependent.

• Once the response statistics are quantified, they are further used to model the level crossing problem. This is one of the important aspects of blade design against excessive deformation as it can hit the tower with catastrophic consequences. In this context, the numerical results presented in this paper clearly shows the response is Gaussian and hence, the crossing rate can be modelled using Rice formula, where the failure can be modelled as a Poisson process. It is observed that the proposed control strategy can significantly enhance the reliability of the turbine blade. Hence, it can be used as an alternative to tilting the rotor and blade, which brings in additional stress at the blade root, bedplate and gear tooth.

Based on the above observations, it can be concluded that the proposed longitudinal stiffening using SMA tendon can control the blade response in both out-of-plane and in-plane direction, offering significant reduction of peak, mean and RMS values. Its impact on the reliability of the blade under serviceability is remarkable. As the blade deforms less, its performance against the ultimate limit state and fatigue life is bound to improve.

References

Agarwala, R. and Ro, P.I. (2015), “Separated pitch control at tip: Innovative blade design explorations for large MW wind turbine blades”, *J. Wind Energy*, **2015**(895974), 1-12. https://doi.org/10.1155/2015/895974.

Anderson, P.M. and Bose, A. (1983), “Stability simulation of wind turbine systems”, *IEEE Trans. Power Appar. Syst.*, **12**, 3791-3795. https://doi.org/10.1109/mper.1983.5520133.

Antoni, J., Bonnardot, F., Raad, A. and El Badaoui, M. (2004), “Cyclostationary modelling of rotating machine vibration signals”, *Mech. Syst. Signal Process.*, **18**(6), 1285-1314. https://doi.org/10.1016/s0888-3270(03)00088-8.

Berg, D.E., Wilson, D.G., Resor, B.R., Barone, M.F., Berg, J.C., Kota, S. and Ervin, G. (2009), “Active aerodynamic blade load control impacts on utility-scale wind turbines (No. SAND20092650C)”, Sandia National Lab (SNL-NM), USA.

Bossanyi, E.A. (2003a), “Individual blade pitch control for load reduction”, *Wind Energy*, **6**(2), 119-128. https://doi.org/10.1002/we.76.

Bossanyi, E.A. (2003b), “Wind turbine control for load reduction”, *Wind Energy*, **6**(3), 229-244. https://doi.org/10.1002/we.95.

Bottasso, C.L., Croce, A., Gualdoni, F. and Montinari, P. (2016), “Load mitigation for wind turbines by a passive aeroelastic device”, *J. Wind Eng. Ind. Aerodyn.*, **148**, 57-69. https://doi.org/10.1016/j.jweia.2015.11.001.

Branner, K. and Ghadirian, A. (2014), “Database about blade faults”, Ph.D. Dissertation, *DTU Wind Energy*, Denmark.

Burton, T., Jenkins, N., Sharpe, D. and Bossanyi, E. (2011), *Wind Energy Handbook*, John Wiley & Sons, Chichester, West Sussex, UK. https://doi.org/10.1002/9781119992714.

Chaari, F. and Haddar, M. (2014), *Cyclostationarity: Theory and Methods*, Springer, Zurich, Switzerland. https://doi.org/10.1007/978-3-319-04187-2_8.

Chan, Y.T. (1995), *Wavelet Basics*, Springer, Boston, USA. https://doi.org/10.1007/978-1-4615-2213-3.

Cheng, T.H., Ren, M., Li, Z.Z. and Shen, Y.D. (2015), “Vibration and damping analysis of composite fiber-reinforced wind blade with viscoelastic damping control”, *Adv. Mater. Sci. Eng.*, **2015**(146949), 1-6. https://doi.org/10.1155/2015/146949.

Das, S., Sajeer, M. and Chakraborty, A. (2019), “Vibration control of horizontal axis offshore wind turbine blade using SMA stiffener”, *Smart Mater. Struct.*, **28**(9), 095025. https://doi.org/10.1088/1361-665x/ab1174.

Dimitrov, N.K., Staerdahl, J., Friis-Hansen, P. and Berggreen, C. (2013), “Structural reliability of wind turbine blades: Design methods and evaluation”, Ph.D. Dissertation, Technical University of Denmark, Kongens Lyngby, Denmark.

DNVGL-ST-0376 (2015), Rotor Blades for Wind Turbines, DET Norsk Veritas.

Fitzgerald, B., Sarkar, S. and Staino, A. (2018), “Improved reliability of wind turbine towers with active tuned mass dampers (ATMDs)”, *J. Sound Vib.*, **419**, 103-122. https://doi.org/10.1016/j.jsv.2017.12.026.

Fitzgerald, B., Staino, A., and Basu, B. (2019), “Wavelet-based individual blade pitch control for vibration control of wind turbine blades”, *Struct. Control Health Monit.*, **26**(1), e2284. https://doi.org/10.1002/stc.2284.

Gardner, W.A. (1994), “Cyclostationarity in communications and signal processing”, *Statistical Signal Processing Inc.* Yountville, USA.

Gardner, W.A., Napolitano, A. and Paura, L. (2006), “Cyclostationarity: Half a century of research”, *Signal Process*, **86**(4), 639-697. https://doi.org/10.1016/j.sigpro.2005.06.016.

Haghdoust, P., Cinquemani, S. and Conte, A.L. (2018), “Preliminary studies on SMA embedded wind turbine blades for passive control of vibration”, *Proceedings of the Active and Passive Smart Structures and Integrated Systems SPIE*, California, USA, August.

Harris, M., Hand, M. and Wright, A. (2006), “Lidar for turbine control”, Report No. NREL/TP-500-39154, National Renewable Energy Laboratory, Colorado, USA. https://doi.org/10.2172/881478.

Holm, S., Josefson, B.L., DeMar, J. and Svensson, T. (1995), “Prediction of fatigue life based on level crossings and a state variable”, *Fatigue Fract. Eng. Mater. Struct.*, **18**(10), 1089-1100. https://doi.org/10.1111/j.1460-2695.1995.tb00841.x.

IEC 61400-1 (2005), Wind Turbines Part 1: Design requirements, International Electrotechnical Commission, UK. https://doi.org/10.3403/30095699.

Jiang, Z., Hu, W., Dong, W., Gao, Z. and Ren, Z. (2017), “Structural reliability analysis of wind turbines: A review”, *Energies*, **10**(12), 1-25. https://doi.org/10.3390/en10122099.

Jonkman, B.J. (2009), “TurbSim user’s guide”, Report No. NREL/TP500-46198, National Renewable Energy Laboratory, Golden, Colorado, USA. https://doi.org/10.2172/965520.

Jonkman, J.M. and Buhl Jr, M.L. (2005), “Fast user’s guide”, Report No. NREL/TP-500-38230, *National Renewable Energy*

Laboratory, Golden, Colorado, USA. https://doi.org/10.2172/15020796.

Jonkman, J., Butterfield, S., Musial, W. and Scott, G. (2009), "Definition of a 5-MW reference wind turbine for offshore system development", Report No. NREL/TP-50038060, National Renewable Energy Laboratory, Golden, Colorado, USA. https://doi.org/10.2172/947422.

Küçük, M., Çetin, N.S. and Emeksiz, C. (2012), "Stress analysis of shape memory alloys used in wind turbine blade root connection", *Energy Edu. Sci. Technol. Part A Energy Sci. Res.*, **30**, 667-676.

Lachenal, X., Daynes, S. and Weaver, P.M. (2013), "Review of morphing concepts and materials for wind turbine blade applications", *Wind Energy*, **16**(2), 283-307. https://doi.org/10.1002/we.531.

Lackner, M.A. (2013), "An investigation of variable power collective pitch control for load mitigation of floating offshore wind turbines", *Wind Energy*, **16**(3), 435-444. https://doi.org/10.1002/we.1500.

Liang, C. and Rogers, C.A. (1997), "One-dimensional thermomechanical constitutive relations for shape memory materials", *J. Intell. Mater. Syst. Struct.*, **8**(4), 285-302. https://doi.org/10.1177/1045389x9700800402.

Liu, L., Bian, H., Du, Z., Xiao, C., Guo, Y. and Jin, W. (2019), "Reliability analysis of blade of the offshore wind turbine supported by the floating foundation", *Compos. Struct.*, **211**, 287-300. https://doi.org/10.1016/j.compstruct.2018.12.036.

Lutes, L.D. and Sarkani, S. (2004), *Random Vibrations: Analysis of Structural and Mechanical Systems*, Elsevier, Burlington, USA. https://doi.org/10.1016/B978-0-7506-7765-3.X5000-2.

Ma, Z., Liu, Y., Wang, D., Teng, W. and Kusiak, A. (2017), "Cyclostationary analysis of a faulty bearing in the wind turbine", *J. Solar Energy Eng.*, **139**(3), 031006. https://doi.org/10.1115/1.4035846.

Ma, Y., Martinez-Vazquez, P. and Baniotopoulos, C. (2019), "Wind turbine tower collapse cases: A historical overview", *Proceedings of the Institution of Civil Engineers-Structures and Building*, London, UK, August. https://doi.org/10.1680/jstbu.17.00167.

Maheswari, R.U. and Umamaheswari, R. (2017), "Trends in non-stationary signal processing techniques applied to vibration analysis of wind turbine drive train - a contemporary survey", *Mech. Syst. Signal Process.*, **85**(2017), 296-311. https://doi.org/10.1016/j.ymssp.2016.07.046.

McCormick, A.C. and Nandi, A.K. (1998), "Cyclostationarity in rotating machine vibrations", *Mech. Syst. Signal Process.*, **12**(2), 225-242. https://doi.org/10.1006/mssp.1997.0148.

Nelson, R., Corke, T., Othman, H., Patel, M., Vasudevan, S. and Ng, T. (2008), "A smart wind turbine blade using distributed plasma actuators for improved performance", *Proceedings of the 46th AIAA Aerospace Sciences Meeting and Exhibit*, Nevada, USA, January. https://doi.org/10.2514/6.2008-1312.

Rao, A., Srinivasa, A.R. and Reddy, J.N. (2015), *Design of Shape Memory Alloy (SMA) Actuators*, Springer, Texas, USA. https://doi.org/10.1007/978-3-319-03188-0.

Rehman, S., Alam, M., Alhems, L.M. and Rafique, M.M. (2018), "Horizontal axis wind turbine blade design methodologies for efficiency enhancement - a review", *Energies*, **11**(3), 1-34. https://doi.org/10.3390/en11030506.

Sarkar, S. and Chakraborty, A. (2017), "Optimal design of semiactive MRTLCD for along-wind vibration control of horizontal axis wind turbine tower", *Struct. Control Health Monit.*, **25**(2), 1-18. https://doi.org/10.1002/stc.2083.

Sarkar, S., Chen, L., Fitzgerald, B., and Basu, B. (2020), "Multi-resolution wavelet pitch controller for spar-type floating offshore wind turbines including wave-current interactions", *J. Sound Vib.*, **470**, 115170. https://doi.org/10.1016/j.jsv.2020.115170.

Shahin, A.R., Meckl, P.H. and Jones, J.D. (1997), "Modeling of SMA tendons for active control of structures", *J. Intell. Mater. Syst. Struct.*, **8**(1), 51-70. https://doi.org/10.1177/1045389x9700800106.

Teng, W., Ding, X., Zhang, Y., Liu, Y., Ma, Z. and Kusiak, A. (2017), "Application of cyclic coherence function to bearing fault detection in a wind turbine generator under electro-magnetic vibration", *Mech. Syst. Signal Process.*, **87**, 279-293. https://doi.org/10.1016/j.ymssp.2016.10.026.

Thomas, F.O., Corke, T.C., Iqbal, M., Kozlov, A. and Schatzman, D. (2009), "Optimisation of dielectric barrier discharge plasma actuators for active aerodynamic flow control", *AIAA J.*, **47**(9), 2169-2178. https://doi.org/10.2514/1.41588.

Van Dam, C.P., Berg, D.E. and Johnson, S.J. (2008), "Active load control techniques for wind turbines", *Sandia Nat. Lab.*, **2008**(4809), 1-132. https://doi.org/10.2172/943932.

Wang, W., Caro, S., Bennis, F. and Mejia, O.R.S. (2014), "A simplified morphing blade for horizontal axis wind turbines", *J. Solar Energy Eng.*, **136**(1), 011018. https://doi.org/10.1115/1.4025970.

Wilson, D.G., Berg, D.E., Zayas, J.R. and Lobitz, D.W. (2008), "Optimised active aerodynamic blade control for load alleviation on large wind turbines", *Sandia Nat. Lab.*, **2008**(4202), 1-7.

BS

Table 5 Mass matrix

Element	Orientation	Equation
Blade	Out-of-plane	$M(i+3,i+3)=\int_0^R m_b(r)\Phi_{i+3}^2 dr$
	In-plane	$M(i,7)=\mathrm{M}(7,i)=\int_0^R m_b(r)\Phi_i dr$
Coupling (B-T)	Out-of-plane	$M(i+3,8)(t)=\mathrm{M}(8,i+3)(t)=\int_0^R m_b(r)\Phi_{i+3}\cos\overline{\psi_\iota}\, dr$
	In-plane	$M(7,7)=3\int_0^R m_b(r)dr+M_n+\int_0^H m_t(h)\Phi_7^2 dh$
Tower	Out-of-plane	$M(8,8)=3\int_0^R m_b(r)dr+M_n+\int_0^H m_t(h)\Phi_8^2 dh$
	In-plane	$M(i+3,i+3)=\int_0^R m_b(r)\Phi_{i+3}^2 dr$

Table 6 Damping matrix

Element	Orientation	Equation
Blade	Out-of-plane	$C(i,i)=2\xi_i\omega_i M(i,i)$
	In-plane	$C(i+3,i+3)=2\xi_{i+3}\omega_{i+3}M(i+3,i+3)$
Tower	Out-of-plane	$C(7,7)=2\xi_7\omega_7 M(7,7)$
	In-plane	$C(8,8)=2\xi_8\omega_8 M(8,8)$

A. System matrices

The non-zero elements of 8 × 8 mass, damping and stiffness matrices of the combined blade-tower system are given in Table 5, where $\overline{\psi_\iota}=\Omega t+(i-1)\frac{2\pi}{3}$ and i = 1, 2, 3. The first subscripts b, t and n represent blade, tower and nacelle respectively.

The damping matrix of the wind turbine system is evaluated using the damping ratio of the blade and tower. In addition to the damping given in Table 6, the damping due to the kinetic energy of a rotating blade is

$$C(8,i+3)(t)=-2\Omega\int_0^R m_b(r)\Phi_{i+3}\sin\overline{\psi_\iota}\, dr \tag{27}$$

The stiffness matrix of the wind turbine system is given in Table 7, where the superscripts e, c, g and T in the above table represent elastic, centrifugal, gravitational and tension in the cable, respectively while subscripts 'out' and 'in' represent the out-of-plane and in-plane directions. $F_c(r)$ and $F_g(r)$ are the centrifugal force due to the rotation of the blade and force due to gravity, which are evaluated as follows

$$F_c(r)=\Omega^2\int_r^R m_b(x)x dx \tag{28a}$$

Table 7 Stiffness matrix

Element	Orientation	Equation
Blade	Out-of-plane	$K(i,i)(t)=K_{out}^e+K_{out}^c+K_{out}^g(t)+K_{out}^T(t)$ $K(i,i)(t)=\int_0^R EI_f\Phi''^2_i dr+\int_0^R\left[F_c(r)+F_g(r)\cos\overline{\psi_\iota}+F_T(t)\right]\Phi'^2_i\, dr$
	In-plane	$K(ii,ii)(t)=K_{in}^e+K_{in}^c+K_{in}^g(t)+K_{in}^T(t)-\Omega^2 M(ii,ii)$ $K(ii,ii)(t)=\int_0^R EI_e\Phi''^2_{ii}dr+\int_0^R\left[F_c(r)+F_g(r)\cos\overline{\psi_\iota}+F_T(t)\right]\Phi'^2_{ii}\, dr-\Omega^2 M(ii,ii)$
Coupling (B-T)	Out-of-plane	$K(i,ii)=K(ii,i)=\int_0^R EI_{fe}\Phi''_i\Phi''_{ii}dr$
	In-plane	$K(8,ii)=-\Omega^2 M(8,ii)$
Tower	Out-of-plane	$K(7,7)=\omega_7^2 M(7,7)$
	In-plane	$K(8,8)=\omega_8^2 M(8,8)$

* [N.B.: *ii*=*i*+3]

$$F_g(r) = -g\int_r^R m_b(x)dx \quad (28b)$$

- Force vector

The blade is exposed to aerodynamic loads and gravitational pull that change with its rotational angle. Therefore, the total force can be expressed as

$$F(t) = Q_w(t) + Q_g(t) \quad (29)$$

where Q_w is the wind load and Q_g is the gravitational load. The gravitational force is always acting downwards. Therefore, the out-of-plane component of this load is equal to zero. The load due to gravitational force given as follows

$$Q_g(t) = \{0 \quad 0 \quad 0 \quad 0 \quad Q_{g_1}^{in} \quad Q_{g_2}^{in} \quad Q_{g_3}^{in} \quad 0\}^T \quad (30)$$

It can be noted that the resultant of the gravitation load acting at the top of the tower along the in-plane direction is zero, as the loads from the blades cancel each other.

$$Q_{g_i}^{in} = F_g\Phi_{i+3}\sin\overline{\psi_\iota} \quad (31)$$